Hindawi
Journal of Nanomaterials
Volume 2022, Article ID 9393188, 10 pages
https://doi.org/10.1155/2022/9393188

Research Article

Application of Spectroscopy Technology in Nanomaterials in Identification of Chinese Paintings

Lili Bai[1], **Heung Kou**[2] **and Zi Kong**[3]

[1]*College of Fine Arts and Design, Nanning Normal University, Nanning, 530100 Guangxi, China*
[2]*Faculty of Arts and Education, Sehan University, Jeollanam-Do, 57447 Mokpo, Republic of Korea*
[3]*Chinese Women Painters Association, China National Academy of Painting, Beijing, 100048 Beijing, China*

Correspondence should be addressed to Heung Kou; sehan668nn@163.com

Received 21 March 2022; Revised 27 April 2022; Accepted 16 May 2022; Published 27 May 2022

Academic Editor: Awais Ahmed

The authenticity of calligraphy and painting is an important knowledge in the collection and research of Chinese painting and calligraphy. The identification of folk painting and calligraphy is usually conducted by experts and scholars engaged in cultural relics, archaeology, painting and calligraphy, and ancient buildings. Relying only on the identification of experience and literature and history, there are certain limitations, and it is difficult to form convincing. Spectroscopic technology mainly uses the characteristic spectral lines of molecules or atoms to judge the chemical composition and relative content of substances, so that different molecular structures of substances can be determined and distinguished; thus, it becomes an effective tool for exploring the molecular structure of substances; therefore, it has been widely used in nanomaterials, biomedicine, cultural relic identification, and other fields. Raman spectroscopy is the most common spectroscopic technique in scattering spectroscopy. When light passes through a material surface, in addition to light transmission and light absorption, light scattering can also be observed. In addition to the original incident light frequencies (Rayleigh scattering and Tyndall scattering), the scattered light also includes some new frequencies, which are called Raman scattering, and its spectrum is Raman spectrum. In this paper, Raman spectroscopy is used to study nanomaterials and calligraphy and painting, and the Raman spectra of real and fake calligraphy and painting, as well as the light absorption rate and degradation rate of nanomaterials at different temperatures, are analyzed experimentally. The results show that the Raman spectrum of the authentic calligraphy reaches the maximum when the wave number is 1000; the peak of the Raman spectrum of the authentic fresco reaches the maximum when the wave number is 1400. The average light absorption rate of nanomaterials in was 47.2%, and the average catalytic degradation rate was 53.6%; the average light absorption rate of nanomaterials was 68.9%, and the average catalytic degradation rate was 62.4%. There are obvious differences in peak shape, peak intensity, peak frequency, etc. between genuine and fake calligraphy and painting. The spectrum of genuine works has good consistency, so the authenticity of calligraphy and painting can be distinguished according to the difference between the spectrums.

1. Introduction

Indian scientists discovered the Raman scattering effect in 1928 [1]. In the following decades, due to the weak intensity of Raman scattered light and the low energy of the excitation light source mercury arc lamp, it has not been widely used in practice. Until the emergence of laser Raman spectrometer and Fourier transform technology, people can use laser as a light source to study the vibrational state of molecules more comprehensively and provide more information on molecular structure, which greatly improves the detection sensitivity of Raman spectroscopy. Subsequently, the application fields of Raman spectroscopy have become increasingly extensive, and special seminars on Raman spectroscopy in various disciplines (medicine, geology, biology, etc.) will be held at the biennial International Raman Spectroscopy Conference. The application range of Raman spectroscopy covers optics, quantum mechanics, electromagnetism, group theory, molecular spectroscopy, and other disciplines and has been widely used in materials, chemical industry, petroleum, polymer, biology,

environmental protection, geology, and other fields. This paper mainly focuses on the application of Raman spectroscopy in the identification of calligraphy and painting and nanomaterials.

The art of Chinese painting and calligraphy is the crystallization of five thousand years of Chinese civilization and a historical treasure in the process of Chinese social development. It reflects the real life of ancient Chinese people from many fields, embodies the unique philosophical concepts and aesthetic concepts of the Chinese nation, and is a material for studying the history of human society. Through the analysis of calligraphy and painting works, we can understand the background information of the era of calligraphy and painting creation, brush and ink skills and drawing methods, as well as the subjective emotions that the author wants to convey, thereby inferring the era of painting and calligraphy, the development of painting technology, and the identification and restoration of painting and calligraphy. When analyzing calligraphy and painting works, the first task is to protect the integrity of the calligraphy and painting. The structure of some works is very complex, and the old ones have even been worn and faded, which makes it difficult to identify calligraphy and painting works. Raman spectroscopy reflects the molecular properties of substances, which will not cause any damage to the object, and requires a small amount of samples. It has the characteristics of fingerprint rapidity, sensitivity, and simplicity. Therefore, Raman spectroscopy has been widely used in the identification and research of calligraphy and painting. In this paper, Raman spectroscopy was used to identify Chinese paintings and calligraphy and to study the light absorption properties and catalytic activity of nanomaterials. Combining traditional Chinese painting and calligraphy with modern advanced technology, new concepts and ideas are used in the current calligraphy and painting appraisal, so that calligraphy and painting can be appraised and appreciated more accurately and objectively, and the authenticity of calligraphy and painting can be identified, to make a reasonable value judgment on the artistry of calligraphy and painting and improve the overall level of the appraisal and appreciation of calligraphy and painting. It provides some feasible references for calligraphy and painting researchers and has certain positive significance for the collection, protection, and research of calligraphy and painting.

2. Related Work

In terms of theoretical research, experts and scholars at home and abroad have discussed the application and development prospects of spectroscopy technology in various fields and have done related research in the application of nanomaterials. Gallas et al. investigated five silica samples by infrared spectroscopy and a homemade thermogravimetric infrared spectroscopy (TG-IR) apparatus to quantify and compare the affinity of these five silicas for water. TG-IR measurements allow precise determination of the molar absorption coefficient, which is independent of the source of the sample and the concentration of silanol groups on the silicon. Experiments showed that the accessibility decreased with the increase of alcohol content, and the silica samples changed linearly with the concentration of adsorbed water [2]. Gibson et al. analyzed NICMOS transmission spectra using a residual permutation algorithm and found that previously published transmission spectra could be restored when the same model was used for system effects, and that the transmission spectra changed considerably when the instrument model was changed slightly. They concluded that NICMOS transmission spectroscopy is highly influenced by the system model and cannot be used as a robust detection of molecules [3]. Bunker et al. studied the long K-band spectrum to measure the star formation rate in the system, searching for eight damped absorber emission values for $z > 2$. Under two different simplifying assumptions, (1) assuming a large disk, the spatial density of DLA at $z = 2.3$ is equal to the spatial density of present-day spiral galaxies. (2) In the layering hypothesis, the DLA size at$z = 2.3$is the same as the gas size of the current spiral galaxy. They search for compact emission sources within a solid angle of 11×2.5 arcsec2 for each system. Compared to the previous most sensitive spectral searches, the studied samples were twice as large, the limit was twice as deep, and the measured solid angles were three times larger [4]. Crowther et al. studied the ISO-SWS spectrum of the Wolf-Rayet galaxy NGC 5253 to provide estimates of its stellar population. They used photoionization models and the latest theoretical O star flux distributions to derive the effective stellar temperature and ionization parameters. They assessed the distribution of highly ionized nebula lines in Wolf-Rayet galaxies in an evolutionary synthesis model, distinguishing regions where different infrared fine structure lines are formed [5]. Sasaki et al. used scanning electron microscopy and Fourier transform infrared spectroscopy to analyze the morphological features and chemical composition (Er) of the bone surface after YAG and CO_2 laser ablation. The experimental group was irradiated with continuous YAG and CO_2 lasers, and the position of the conventional micromotor drilling was used as the control group. Fourier transform infrared spectroscopy showed that the chemical composition of the bone surface after YAG laser ablation was basically the same as that after motor drilling. And after laser irradiation, no toxic substances were detected [6]. Yamada et al. investigated the kinetics of room temperature ionic liquid 1-butyl-3-methylimidazolium bis (trifluoromethylsulfonyl) imide (BmimNTf2) using two-dimensional infrared vibrational echo spectroscopy and polarization-selective pump probe. They observed the long-time-scale structural spectral diffusion components at 600 ps, as well as short- and intermediate-time scales for selenocyanate anion (SeCN–) measurements. Experiments have shown that 2-SeCN-Bmim+ is sensitive to local motions in the ionic region, which affect the spectral diffusion and redirection of small, anionic, and neutral molecules [7]. Yan et al. studied solid-phase redox transitions with X-ray spectroscopy and he used high-resolution X-ray spectroscopy (HR-XPS) to observe multivalent arsenic reacting nZVI particles with aqueous As(III). They believe that the morphology of arsenic in the nanoparticles depends largely on the loading of nZVI. Most of the arsenic is found in the reduced state in the nZVI environment, resulting in rapid depletion of Fe(0) cores and arsenic sequestration in oxide formation. Encapsulation of arsenic in most of the solid phase suggests that nZVI is a more powerful arsenic scavenger [8].

3. Spectroscopy and Nanomaterials

3.1. Raman Spectroscopy. Raman scattering effect is an inelastic scattering phenomenon caused by crystal structure, symmetry, charge, and other factors [9]. Raman spectra are significantly different in different substances, so Raman spectra are also called "fingerprints." Based on the Raman effect, qualitative, quantitative, and structural analysis can be performed on the Raman peak position, peak value, line type, line width, and number of spectral lines of the sample. When light enters the surface of an object, most of the light will be transmitted or absorbed, and only 0.1% of the photons will be scattered [10, 11]. During scattering, after the molecule absorbs energy, it will transition from the ground state to the virtual energy level and then drop from the virtual energy level to a lower energy level and release the scattered light. Raman spectroscopy includes optics, quantum mechanics, electromagnetism, molecular structure, molecular spectroscopy, and other disciplines and its applications in chemistry, physics, biology, medicine, environmental science, and other fields. These applications vary in nature, from purely qualitative to highly quantitative.

Light scattering is another natural phenomenon besides light absorption, light reflection, light transmission, and light emission, and it is an interaction between light and matter. Light scattering is caused by the collision of incident photons with objects in a certain direction, and the incident photons are shifted from the original incident direction [12]. Scattered light generally contains information about the structure of matter and is accompanied by changes in energy. It can be divided into elastic scattering and inelastic scattering according to the size of its fall back to the lower energy layer. The so-called elastic scattering, also known as Rayleigh scattering, means that when the excited molecule is deexcited, its energy level returns to the initial energy level, and the scattering energy is equal to the excitation energy. On the other hand, inelastic scattering is Raman scattering. When the excited molecule is deexcited, its energy level returns to the noninitial energy level, and the scattering energy is not the same as the excitation energy. There are two types of Raman scattering: Stokes scattering and anti-Stokes scattering. The energy of Stokes scattering is less than the energy of excitation, and the molecule is deexcited and falls back to an energy level higher than the initial energy level. On the other hand, the energy of anti-Stokes scattering is greater than the energy of excitation, and the molecule falls back to an energy level lower than the initial energy level. Generally, the Stokes scattering intensity is larger than the anti-Stokes intensity [13], and this process is shown in Figure 1.

It can be seen from the transition diagram of the energy level that both Raman scattering and Rayleigh scattering are caused by the transition of the ground state electrons to the virtual state under the excitation of the incident light and then to the ground state and emitting scattered light [14]. In Rayleigh scattering, since the electron does not interact with the phonon, its energy does not change, that is, its scattering frequency does not change with the frequency of the incident light. In Raman scattering, when electrons enter the virtual state, they will interact with phonons, which will cause the loss of phonon energy, resulting in the scattered light energy being smaller or greater than the incident light energy. That is, the frequency of scattered light decreases or increases by $\Delta\nu$ compared with the frequency of incident light, which corresponds to the Stokes or anti-Stokes Raman scattering process, respectively.

Raman scattering spectrum is a form of reflecting Raman shift, that is, the wavenumber difference between excitation light and scattered light. Raman scattering, unlike Rayleigh scattering, is a type of inelastic scattering, and in this case, Stokes light as the wavelength increases, and when the wavelength is reduced, it is anti-Stokes light. The principle of Raman scattering is shown in Figure 2. By detecting the scattered photons, Raman spectra can be obtained. Different bands correspond to the vibrational frequencies of different functional groups. Each molecule has a unique spectrum, called a "fingerprint," based on its chemical bonds and its specific vibrational frequency.

Raman spectroscopy is a type of molecular vibrational spectroscopy. It corresponds to the change of intramolecular vibrational energy level, carries information, such as the composition and structure of the substance itself, and has high specificity. It is a good spectral detection method [15]. One of the advantages of Raman spectroscopy is that the excitation light source can be selected at will. From the principle of Raman scattering, it can be seen that the frequency shift of the Raman spectrum has nothing to do with the frequency of the light source, and different light sources can be selected according to different samples. Secondly, Raman scattering is generated by the laser, which has strong directivity and can measure tiny samples in a very small area, thereby realizing long-distance noncontact detection. Since the laser has good monochromatic properties, good orientation ability, and high energy density, using it as an excitation light source can greatly improve the excitation efficiency. Raman spectroscopy does not need to prepare samples and can directly measure the measured objects, such as ancient painting pigments and traces left at crime scenes, so that they can be preserved intact [16]. Third, Raman spectroscopy can identify the chemical composition of cells. This method does not require labeling and staining and allows semiquantitative analysis of proteins, lipids, and DNA through vibrational spectroscopy, which can visually display their intracellular distribution. Fourth, Raman spectroscopy has a wide detection range. Since both polar molecules and nonpolar molecules can form Raman spectra, the detection objects of Raman spectra are very wide, including inorganic substances, organic substances, polymers, minerals, animal and plant tissues, and catalysts.

In spectroscopy, the grating resolution is usually defined as

$$R = \frac{\lambda}{\Delta\lambda} = m \times N. \tag{1}$$

Among them, $\Delta\lambda$ refers to the minimum wavelength difference that the wavelength λ can resolve. m refers to the spectral order, and N is the total number of grating scales. Here, $\Delta\lambda$ depends not only on the resolving power of the dispersing element but also on the construction parameters

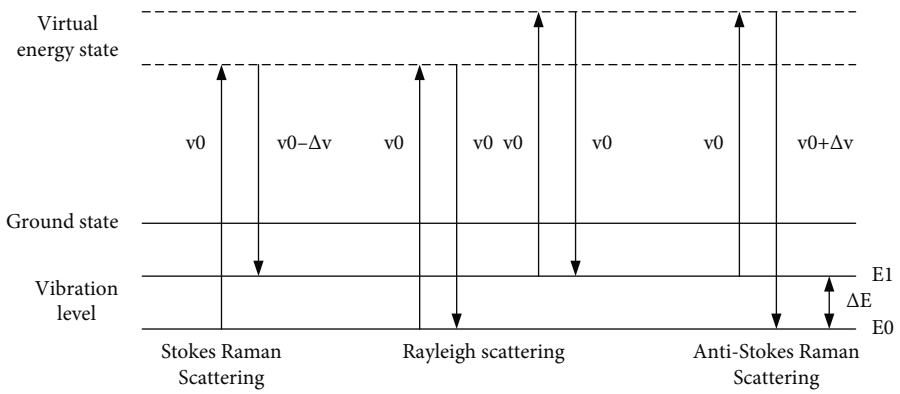

Figure 1: Energy level diagram for scattering process.

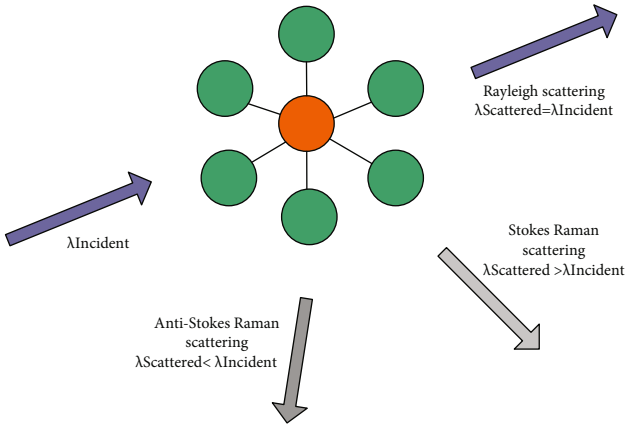

Figure 2: Principles of Raman scattering.

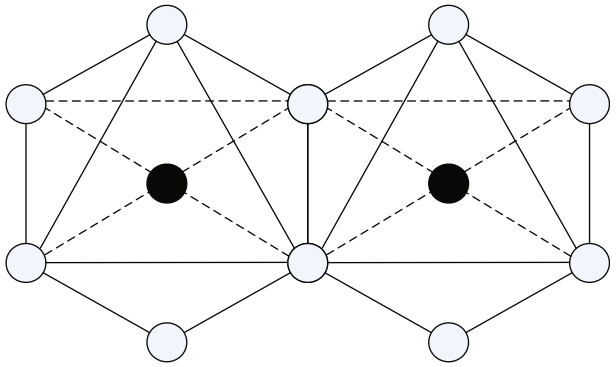

Figure 3: Crystal structure of rutile.

such as the slit size, the focal length of the spectrometer, and the optical quality of the optical components. Increasing the total number of grating lines or increasing the spectral order can improve the spectral resolution. The optical properties of a grating can be described by the following formula:

$$m\lambda = d(\sin i + \sin r). \tag{2}$$

Here, λ refers to the diffraction wavelength, d refers to the grating constant, and i and r refer to the incident angle and diffraction angle, respectively. Clearly, when the incident angle and the diffraction angle are equal, the increase of the incident angle makes the spectral order increase.

At present, to evaluate the quality of Raman spectra, there are mainly methods for estimating the standard deviation of noise, which are discussed below. The random noise in the Raman spectrum is formed by the superposition of many random noise sources, which can be considered to satisfy the Gaussian distribution and belong to the Gaussian noise. Assuming that the Gaussian noise in the original signal is N, its standard deviation is σN, the signal filtered by a high-pass filter G is N', the standard deviation is $\sigma N'$, and the unit impulse response sequence of the high-pass filter is $g(n)$. Then, the power spectral density of N and the spectrum of the high-pass filter are the following formulas, respectively:

$$P(w) = \sigma_N^2, \tag{3}$$

$$G(w) = \sum_{n=-\infty}^{+\infty} g(n)e^{-jnw}, \tag{4}$$

where w represents the digital angular frequency, $w \in [-\pi, \pi]$.

N' is N obtained after being filtered by high-pass filter G, which should satisfy

$$N' = N * G, \tag{5}$$

where a represents a convolution, and its spectrum satisfies

$$F'(w) = F(w) \cdot G(w). \tag{6}$$

Among them, $F(\omega')$ and $F(\omega)$ represent the spectrum of N' and N, respectively. For the power-limited signals N' and N, they are limited in the range of $[-T/2, T/2]$, and their spectrums are ${F_T}'(\omega)$ and $F_T(\omega)$, respectively, which satisfy

$$F_T'(w) = F_T(w) \cdot G(w). \tag{7}$$

When T tends to infinity, the following formula is obtained:

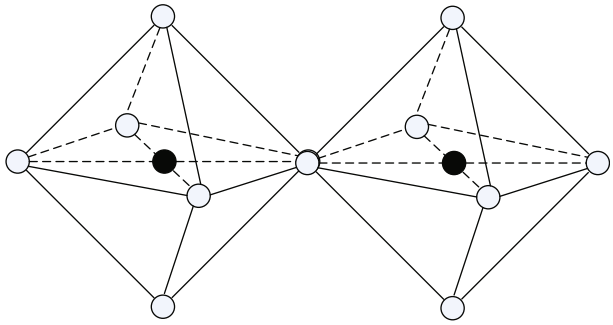

Figure 4: Crystal structure of anatase.

Table 1: Crystal structure parameters of rutile and anatase.

Property	Rutile	Anatase
Crystal system	Tetragonal system	Tetragonal system
Lattice constant	$a = 4.5936$	$a = 3.784$
	$c = 2.9587$	$c = 9.515$
Space group	P42/mnm	I41amd
Molecule number	2	2
Ti-O bond length	1.949 (4)	1.939 (4)
	1.980 (2)	1.965 (2)
O-Ti-O bond angle	81.2°	77.7°
	90.0°	92.6°

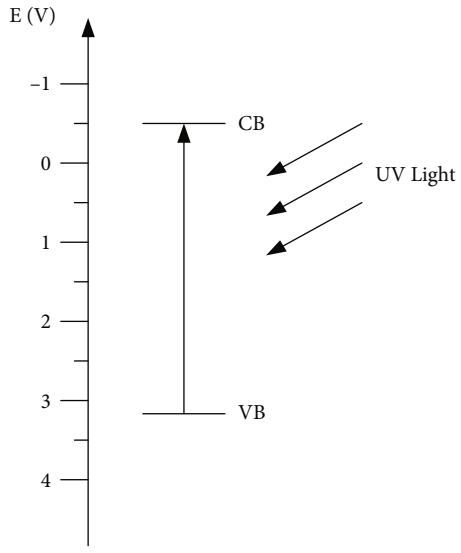

Figure 5: Light reaction mechanism.

$$\lim_{T\longrightarrow\infty} F_T'(w) = G(w) \cdot \lim_{T\longrightarrow\infty} F_T(w). \tag{8}$$

The power spectral density of N' is shown in

$$P'(w) = |G(w)|^2 \cdot \lim_{T\longrightarrow\infty} \frac{1}{T} |F_T(w)|^2. \tag{9}$$

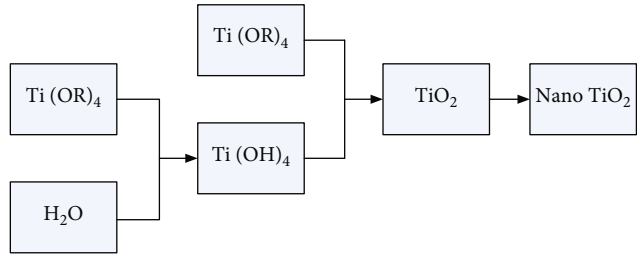

Figure 6: Process flow chart for preparing.

It can get

$$P'(w) = |G(w)|^2 \cdot P(w). \tag{10}$$

Since the autocorrelation function and the power spectrum function are mutual Fourier transforms, the autocorrelation function $R(\tau')$ of the filtered signal N' is shown in

$$R'(\tau) = \frac{1}{2\pi} \int_{-\infty}^{+\infty} P'(w) e^{-jw\tau} dw. \tag{11}$$

Moreover, defined by the power-limited signal autocorrelation function, the following formula is obtained:

$$R'(\tau) = \lim_{T\longrightarrow\infty} \frac{1}{T} \int_{-T/2}^{T/2} N'(t) N'(t+\tau) dt. \tag{12}$$

Let $\tau = 0$, and formula (12) can be transformed into

$$R'(0) = \lim_{T\longrightarrow\infty} \frac{1}{T} \int_{-T/2}^{T/2} \left|N'(t)\right|^2 dt. \tag{13}$$

Since the mean value of the high-pass filtered signal N' is zero, the following formula can be derived.

$$R'(0) = \sigma_N'^{\,2}. \tag{14}$$

Combining formulas (3), (4), (9), (10), (14), it can be deduced that

$$R'(0) = \sigma_N^2 \sum_{n=-\infty}^{+\infty} g^2(n) = \sigma_N^2 \|g\|^2. \tag{15}$$

It can be concluded from the above derivation that the noise variance filtered by a high-pass filter is equal to the noise variance in the original signal multiplied by the square of the modulus of the filter's response vector.

The core idea of the noise standard deviation estimation method is to use the high-pass filtered noise standard deviation to estimate the noise standard deviation in the original signal. Gaussian noise is mainly concentrated in the high-frequency domain. After the original signal is high-pass filtered, the low-frequency signal is filtered out. The high-frequency signal that passes through is mainly noise, and the interference of the signal is very small. At this time, it is more

Table 2: The relationship between hydrolysis reaction temperature and gel time.

Hydrolysis temperature	Gel time
20°C	48~72 h
30°C	30~35 h
40°C	18~20 h
50°C	<8 h

Table 3: Relationship between calcination temperature and average particle size of TiO.

Calcination temperature	Particle size
400°C	48~72 h
500°C	30~35 h
600°C	18~20 h
700°C	<8 h

accurate to calculate the standard deviation of the filtered noise, and then, the standard deviation of the noise in the original signal can be estimated by formula (15).

The specific operation is as follows: set the wavelet coefficients on two adjacent small scales to be $wc_1(n)$、$wc_2(n)$, respectively, and their correlation coefficient to be $\mathrm{Cor}_1(n)$, $n = 1, 2, \cdots L$, where L represents the length of the discrete signal. The correlation coefficient $\mathrm{Cor}_1(n)$ satisfies the

$$Cor_1(n) = wc_1(n) \cdot wc_2(n). \tag{16}$$

Normalizing the energy of $\mathrm{Cor}_1(n)$ so that the energy of the new correlation coefficient $\mathrm{Cor}_2(n)$ is equal to the energy of $wc_1(n)$. Let the energies of $\mathrm{Cor}_1(n)$ and $wc_1(n)$ be E_{Cor_1} and E_{wc_1}, respectively, and formulas (17) and (18) are as follows:

$$E_{cor1} = \sum_{n=1}^{L} |Cor_1(n)|^2, \tag{17}$$

$$E_{wc1} = \sum_{n=1}^{L} |wc_1(n)|^2. \tag{18}$$

The new correlation coefficient $\mathrm{Cor}_2(n)$ can be expressed as

$$Cor_2(n) = Cor_1(n) \cdot \sqrt{E_{wc1}/E_{cor1}}. \tag{19}$$

Comparing $\mathrm{Cor}_2(n)$ with $wc_1(n)$, if the position n_0 satisfies the formula (20), the wavelet coefficient $wc_1(n_0)$ at n_0 is considered to be caused by the signal, and it is set to zero, thus obtaining the small-scale wavelet coefficient $wc'_1(n)$ with the signal interference removed, using formula (15) again, the noise standard deviation of the original signal can be estimated.

$$Cor_2(n_0) \geq |wc_1(n_0)|. \tag{20}$$

3.2. Nanomaterials. Nanomaterials are an emerging material that appeared in the 1980s, usually referring to the particle structure with nanometer size. Because nanoparticles have special properties that are significantly different from individual materials and single molecules, such as size effect, surface effect, volume effect, quantum effect, and macroscopic quantum tunneling effect; therefore, it has a wide range of applications in the fields of electronics, optics, chemical industry, ceramics, biology, and medicine [17, 18]. The preparation, structure, properties, and photocatalytic mechanism of TIOZ materials has been an important topic in the field of photocatalysis since it was discovered in the early 1970s that TIOZ electrodes have the function of splitting water under sunlight. After entering the 1990s, with the rapid development of nanotechnology, nanophotocatalysis technology has been widely used, and its particle size, surface area, and other technologies have also been further developed, and to a certain extent, the improvement of its quantum efficiency is achieved through the design of materials.

Photocatalysis technology is through photocatalysis, and the electrons in the valence band of the semiconductor are excited to transition to the conduction band to form a pair of electrons and holes and react with O_2 and H_2O/OH^- on the surface of the catalyst to generate free radicals, so that the organic compounds are gradually decomposed into small molecular substances such as CO_2 and H_2O. Since the research of semiconductor photocatalytic oxidation technology, many semiconductor catalysts with catalytic effect have been discovered, such as TiO_2, ZnO, SnO_2, Fe_2O_3, $BiVO_4$, Cu_2O, CdS, and C_3N_4 [19]. Among them, TiO_2 is in a leading position among many semiconductor catalysts due to its nontoxic and harmless, strong stability and strong redox ability.

It is a white powder in nature, TiO_2 mainly rutile, anatase, brookite, and TiO_2(B) phase. Generally speaking, the crystalline titanium dioxide prepared at low temperature is anatase and brookite phases, while the rutile phase is stable at high temperature. Among them, the rutile and anatase forms TiO_2 are the most widely used in the field of photocatalysis, and the two crystal forms TiO_2 exhibit different properties due to structural differences. Both rutile type and anatase type TiO_2 are composed of octahedrons with Ti as the center and O as the corner, TiO_6 as the basic unit, and both phases belong to the tetragonal crystal system. The main difference lies in the connection mode between the octahedrons and the degree of lattice distortion [20]. The crystal structure is shown in Figures 3 and 4. The connection between octahedrons is mainly connected by common edges and common corners. In the anatase type TiO_2, each octahedron is connected with the surrounding eight octahedrons (four common edges and four common corners), whereas in the rutile type TiO2, each octahedron is connected to ten surrounding octahedra (two common edges and eight common corners). Because the crystal connection method is different, the degree of crystal distortion of the anatase type is also stronger, so the symmetry and stability of the rutile type TiO_2 lattice are higher than those of the anatase type TiO_2, and in the crystal coordination structure, the more the number of common edges, the worse the stability of the crystal structure. Therefore, the most stable crystal phase of titanium dioxide is the rutile phase, both

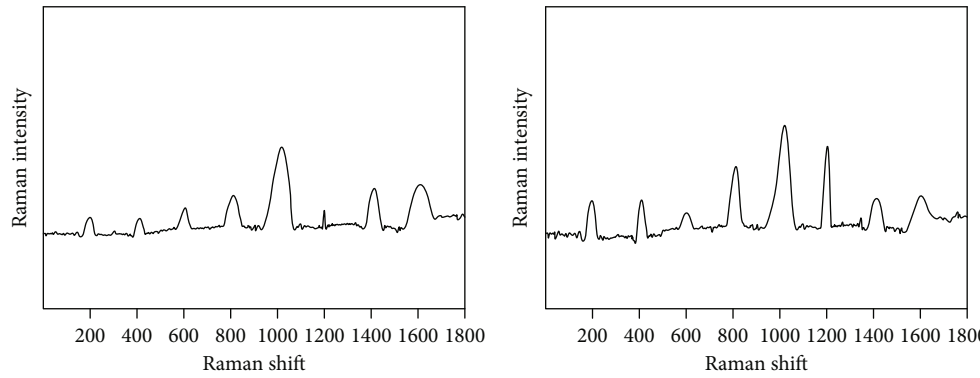

Figure 7: Raman spectra of authentic and fake calligraphy. (a) shows the Raman spectrum of the authentic calligraphy, and (b) shows the Raman spectrum of the calligraphy fake.

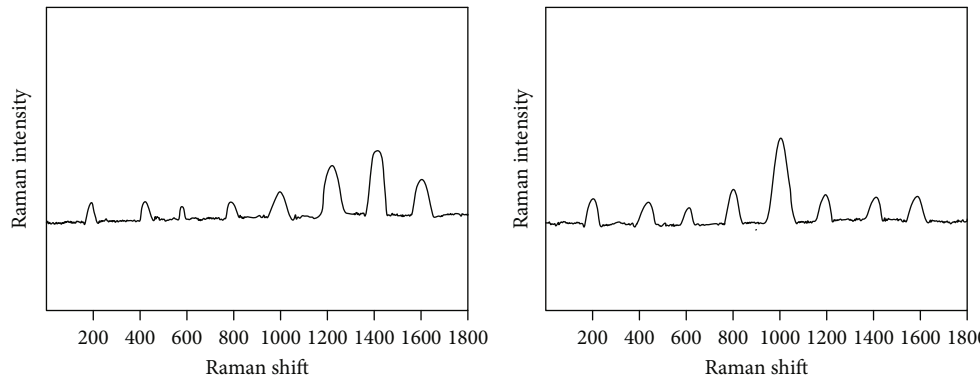

Figure 8: Raman spectra of authentic and fake murals. (a) shows the Raman spectrum of the authentic mural, and (b) shows the Raman spectrum of the fresco fake.

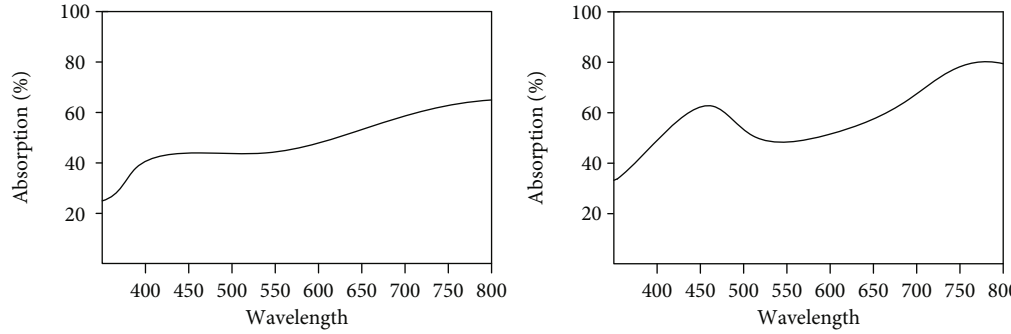

Figure 9: Optical absorptivity of nanomaterials at different temperatures. (a) is the light absorption rate of nanomaterials, and (b) shows the light absorption rate of nanomaterials.

anatase phase and brookite phase can be transformed into rutile phase during high temperature treatment, and this process is generally irreversible at a phase transition temperature of 500-600°C.

Table 1 presents crystallographic data for rutile and anatase types, The Ti-Ti bond distance (3.57 Å) in the rutile phase structure is larger than that in the anatase phase structure (3.79 Å). The Ti-O bond distance (1.949 Å) in the rutile phase structure is shorter than that in the anatase phase structure (1.939 Å). The density of rutile phase TiO_2 material (4.25) is greater than that of anatase phase TiO_2 material (3.89).

Titanium dioxide is a wide-band semiconductor material. The forbidden band width of the anatase phase grain is 3.2 eV, the forbidden bandwidth of the rutile phase grain is 3.02 eV, and the forbidden band width of the brookite phase grain is 2.96 eV. The valence band of TiO_2 includes the 3d orbital of Ti and the 2p orbital of O, while the conduction band only includes the 3d orbital of Ti [21]. When TiO_2 is irradiated with a light beam with a wavelength below

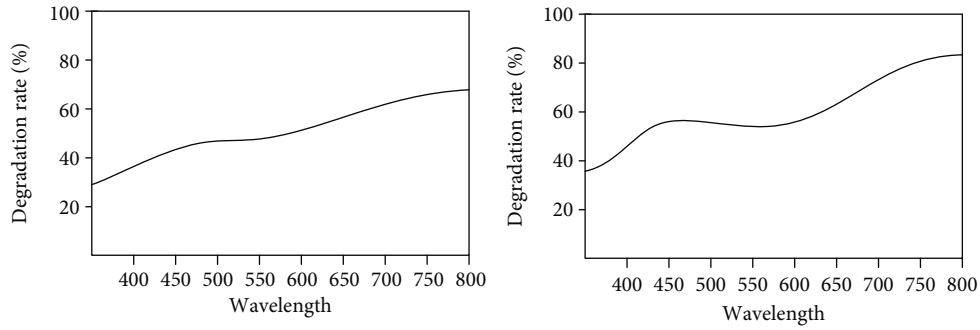

Figure 10: Photocatalytic activity of nanomaterials at different temperatures. (a) shows the photocatalytic degradation rate of nanomaterials, and (b) shows the photocatalytic degradation rate of nanomaterials.

Table 4: Photocatalytic reaction rates at different voltages.

TiO_2	Voltage	2 h	4 h	6 h	8 h	10 h
	25 V	1.12	1.46	1.71	2.27	2.70
Reaction speed	35 V	1.29	2.05	2.11	2.65	2.34
	45 V	1.69	2.23	2.50	2.23	2.06

387 nm, the electrons in its valence band are excited into the conduction band, thereby forming an energy-efficient electron e^- with a negative charge, and form a hole h^+ with a punctual point in the valence band. The reaction principle is shown in Figure 5.

The sol-gel method uses titanium alkoxides or inorganic salts as precursors to form sols through the hydrolysis reaction of the precursors, and the hydrolyzed precursors are further condensed to form gels, and finally, the desired materials are prepared by drying and heat treatment. The process is shown in Figure 6. Tetrabutyl titanate is hydrolyzed in water or alcohols to form oligomers, and the oligomers interact and polymerize to form a three-dimensional network structure with Ti-O-Ti as the polymer unit. At the beginning of the chemical reaction, a large number of small molecules are formed by hydrolysis and polymerization. They form long molecular chains through polymerization, and cross-linking and branching occur between the long molecular chains and small molecules, forming two-dimensional, three-dimensional, and even multidimensional networks and then forming gels. Among them, the morphology, size, crystallinity, and surface properties of the gel particles are affected by the components of the solution, pH, reaction temperature, and other factors. The size, morphology, crystallinity, and surface properties of nano-TiO_2 particles can be regulated by controlling the experimental conditions. The relationship between the hydrolysis reaction temperature and the gelation time is shown in Table 2.

Finally, the organic components of the gel are removed through heat treatment processes such as drying and calcination to obtain nano-TiO_2. The relationship between the calcination temperature and the average particle size of TiO_2 is shown in Table 3. Generally speaking, when the polymer chain has obvious branching and cross-linking, there are a lot of holes in the colloid, and it has good structural stability. However, when the branching and cross-linking of the colloid chain is not obvious, the pores in the colloid are not large, the structure will be relatively fragile, and it is easy to break during the calcination process.

4. Experiment of Spectroscopic Technique in Chinese Painting Identification

Using Raman spectroscopy technology, two authentic calligraphy and mural paintings and their fakes during the Song Dynasty were analyzed, and their respective Raman spectra were obtained, as shown in Figures 7 and 8. Figure 7 shows the Raman spectra of genuine calligraphy and fakes. Figure 8 shows the Raman spectra of the original and fake murals.

Through the analysis of Figure 7, it can be seen that the Raman spectra of genuine and fake calligraphy are significantly different. The calligraphic authentic Raman spectrum has peaks at 200, 400, 600, 800, 1000, 1200, 1400, and 1600 in the 0-1800 cm^{-1} wavenumber range. And when the wave number is 1000 cm^{-1}, the peak is the largest, followed by the peaks at 1400 and 1600 cm^{-1}. The Raman spectrum of the calligraphic fake also has peaks at 200, 400, 600, 800, 1000, 1200, 1400, and 1600 in the wavenumber range of 0-1800 cm^{-1}. Different from the real one, the fake Raman spectral peaks are concentrated between 800 and 1200 cm^{-1}.

By analyzing Figure 8, it can be seen that the Raman spectra of the authentic and fake murals are significantly different. The authentic Raman spectrum of the fresco has peaks at 200, 400, 600, 800, 1000, 1200, 1400, and 1600 in the 0-1800 cm^{-1} wavenumber range. When the wave number is 1400 cm^{-1}, the peak value is the largest, followed by the peak value at 1200 and 1600. The Raman spectrum of the fresco fake also has peaks at 200, 400, 600, 800, 1000, 1200, 1400, and 1600 cm^{-1} in the wavenumber range of 0-1800 cm^{-1}. Unlike the real one, the fake Raman spectrum peaks around 1000 cm^{-1}.

By selecting Rhodamine B as a typical photocatalytic degradation research object, the test of the degradation ability of the nanomaterial TiO_2 sample is characterized. The test results are shown in Figures 9 and 10. Figure 9 shows the light absorptivity of nanomaterials at different temperatures. Figure 10 shows the photocatalytic degradation rates of nanomaterials at different temperatures.

Through the analysis of Figure 9, it can be known that the absorption rate of TiO_2 with light is different at different temperatures. When the temperature is 400°C, the light absorption rate of TiO_2 with a wavelength of 800 nm is the highest, reaching 64.9%. The light absorption rate for the wavelength of 400~600 nm is basically the same, which is maintained at about 42.1%; the light absorption rate for the wavelength of 600~800 nm increases steadily. When the temperature is 600°C, TiO_2 has the highest absorption rate of light with a wavelength of 780 nm, reaching 80.4%. The absorption rate of light with a wavelength of 400 nm is 48.7%, and the absorption rate of light with a wavelength of 450 nm is 61.2%; the absorption rate of light with a wavelength of 550~750 nm increases from the initial 53.2% to 79.5%.

From the analysis of Figure 10, it can be seen that the catalytic degradation rate of TiO_2 to light varies greatly at different temperatures. When the temperature is 400° C the catalytic degradation rate of light with a wavelength of 450 nm is 41.7%, and the catalytic degradation rate of light with a wavelength of 650 nm is 58.3%. When the temperature is 600° C the catalytic degradation rate of light with a wavelength of 450 nm was 54.6%, and the catalytic degradation rate of light with a wavelength of 650 nm was 64.3%.

Exploring the photocatalytic activity of nanomaterials involves two parameters: photocatalytic degradation rate and reaction rate. In addition to the photocatalytic degradation rate, the reaction rate should also be studied. Table 4 shows the photocatalytic reaction rates of nanomaterials at different voltages.

It can be seen from Table 4 that when the voltage is 25 V, the best photocatalytic activity appears in the TiO_2 nanomaterials prepared under the condition of 10 h, and its reaction rate constant is 2.70×10^{-3} min^{-1}. When the voltage is 35 V, the best photocatalytic activity appears in the TiO_2 nanomaterials prepared under the condition of 8 h, and the reaction rate constant is 2.65×10^{-3} min^{-1}. When the voltage is 45 V, the best photocatalytic activity appears in the TiO_2 nanomaterials prepared under the condition of 6 h, and its reaction rate constant is 2.50×10^{-3} min^{-1}. At the same voltage, the reaction rate constant first increases and then decreases with time.

5. Conclusion

An important part of the identification of calligraphy and painting is to identify the authenticity, and the identification of the authenticity of calligraphy and painting has always been a major subject of Chinese painting and calligraphy collection and research. In the identification of calligraphy and painting, Raman spectroscopy is used increasingly. Using Raman spectroscopy to assist in the identification of cultural relics can not only speed up the identification but also reduce the artificiality and subjectivity in the identification process, improve the accuracy and objectivity of identification, reduce the probability of errors in identification, and shorten the identification time. After spectral analysis, the spectra of genuine and fake calligraphy and painting have great differences in peak shape, intensity, and frequency, and the spectrum of genuine works shows good consistency, so that the authenticity can be distinguished from the difference in the spectra. The use of spectral technology can not only ensure the accuracy of identification but also prevent damage to calligraphy and painting. Therefore, Raman spectroscopy is a nondestructive and accurate in situ analysis method, which is suitable for the precise analysis of antiques, calligraphy, and painting. The application of Raman spectroscopy technology in cultural relics, calligraphy, and painting has enriched the identification methods of cultural relics, calligraphy, and painting and improved its scientificity and credibility. With the advancement of science and technology, spectroscopic technology will be an important method of calligraphy and painting identification. However, in-depth study of calligraphy and painting identification requires research on this paper. By observing the scanning electron microscope image of the rice paper, we can analyze the general proportion of leather and grass in the paper from the structure of the surface of the rice paper or the number of long and short fibers in the paper and further use this method to identify the year and type of the rice paper.

Data Availability

The data underlying the results presented in the study are available within the manuscript.

Conflicts of Interest

The authors declare that they have no conflicts of interest.

References

[1] L. Ping, J. A. Rodriguez, and T. Asakura, "Desulfurization reactions on Ni2P(001) and alpha-Mo2C (001) surfaces: complex role of P and C sites," *The Journal of Physical Chemistry B*, vol. 109, no. 10, pp. 4575–4583, 2017.

[2] J. P. Gallas, J. M. Goupil, A. Vimont et al., "Quantification of water and silanol species on various silicas by coupling IR spectroscopy and in-situ thermogravimetry," *Langmuir*, vol. 25, no. 10, pp. 5825–5834, 2009.

[3] N. P. Gibson, F. Pont, and S. Aigrain, "A new look at NICMOS transmission spectroscopy: no conclusive evidence for molecular features," *Monthly Notices of the Royal Astronomical Society*, vol. 6, no. S276, pp. 478-479, 2010.

[4] A. J. Bunker, S. J. Warren, D. L. Clements, G. M. Williger, and P. C. Hewett, "Limits on the star formation rates of z>2 damped Lyα systems from Hα spectroscopy," *Monthly Notices of the Royal Astronomical Society*, vol. 309, no. 4, pp. 875–884, 1999.

[5] P. A. Crowther, S. C. Beck, A. J. Willis, P. S. Conti, P. W. Morris, and R. S. Sutherland, "Properties of hot stars in the Wolf-Rayet galaxy NGC 5253 from ISO-SWS spectroscopy," *Monthly Notices of the Royal Astronomical Society*, vol. 304, no. 3, pp. 654–668, 1999.

[6] K. M. Sasaki, A. Aoki, S. Ichinose, T. Yoshino, S. Yamada, and I. Ishikawa, "Scanning electron microscopy and Fourier transformed infrared spectroscopy analysis of bone removal using Er: YAG and CO_2 lasers," *Journal of Periodontology*, vol. 73, no. 6, pp. 643–652, 2002.

[7] S. A. Yamada, H. E. Bailey, A. Tamimi, C. Li, and M. D. Fayer, "Dynamics in a room-temperature ionic liquid from the cation perspective: 2D IR vibrational echo spectroscopy," *Journal of*

the American Chemical Society, vol. 139, no. 6, pp. 2408–2420, 2017.

[8] W. Yan, M. Ramos, B. E. Koel, and W. X. Zhang, "As(III) sequestration by iron nanoparticles: study of solid-phase redox transformations with X-ray photoelectron spectroscopy," *Journal of Physical Chemistry C*, vol. 116, no. 9, pp. 5303–5311, 2012.

[9] S. Bell and S. Dick, "Quantitative surface-enhanced Raman spectroscopy of single bases in oligodeoxynucleotides," *Faraday Discussions*, vol. 205, no. 5, pp. 517–536, 2017.

[10] R. G. Janssen, J. Duynhoven, and W. Verboom, "Studies on the dynamics of Phosphorylatedp-tert-Butylcalix[6]arenes by using 2D NMR spectroscopy," *Journal of the American Chemical Society*, vol. 118, no. 15, pp. 3666–3675, 1996.

[11] T. B. And and M. Bieri, "Time-resolved in situ ATR spectroscopy of 2-propanol oxidation over Pd/Al 2 O 3: evidence for 2-Propoxide intermediate," *Journal of Physical Chemistry B*, vol. 108, no. 35, pp. 13364–13369, 2017.

[12] G. Poppe, C. Wijers, and A. V. Silfhout, "Ir spectroscopy of CO physisorbed on NaCl (100): microscopic treatment," *Physical Review B: Condensed Matter*, vol. 251, no. 7, pp. 7917–7929, 2017.

[13] C. Li, P. Liu, C. Zou, F. Sun, J. M. Cioffi, and L. Yang, "Spectral-efficient cellular communications with coexistent One- and two-hop transmissions," *IEEE Transactions on Vehicular Technology*, vol. 65, no. 8, pp. 6765–6772, 2016.

[14] M. Puech, H. Flores, F. Hammer, and M. D. Lehnert, "3D spectroscopy with VLT/GIRAFFE," *Astronomy & Astrophysics*, vol. 455, no. 1, pp. 131–134, 2006.

[15] T. H. Prettyman, N. Yamashita, M. J. Toplis et al., "Extensive water ice within Ceres' aqueously altered regolith: evidence from nuclear spectroscopy," *Science*, vol. 355, no. 6320, pp. 55–59, 2017.

[16] D. J. C. Ji-Yang and V. V. Kumar, "Probing electrochemical interfaces using shell-isolated nanoparticles-enhanced Raman spectroscopy," *Electrochemistry*, vol. 1, no. 1, pp. 16–21, 2017.

[17] B. Gao, X. Ning, and P. Xing, "Shock wave induced nanocrystallization during the high current pulsed electron beam process and its effect on mechanical properties," *Materials Letters*, vol. 237, no. 15, pp. 180–184, 2019.

[18] J. J. Peterson and T. D. Krauss, "Fluorescence spectroscopy of single lead sulfide quantum dots," *Nano Letters*, vol. 6, no. 3, pp. 510–514, 2017.

[19] L. Zeng, J. Shi, J. Luo, and H. Chen, "Silver sulfide anchored on reduced graphene oxide as a high -performance catalyst for CO_2 electroreduction," *Journal of Power Sources*, vol. 398, pp. 83–90, 2018.

[20] N. Bastian, E. Emsellem, M. Kissler-Patig, and C. Maraston, "Young star cluster complexes in NGC 4038/39," *Une chaire de médecine au XVe siècle; un professeur à l'Université de Pavie de 1432 à 1472*, vol. 445, no. 2, pp. 471–483, 2006.

[21] L. S. Rothman, I. E. Gordon, and Y. Babikov, "The HITRAN2016 molecular spectroscopic database," *Journal of Quantitative Spectroscopy & Radiative Transfer*, vol. 130, no. 11, pp. 4–50, 2017.